High Resolution Spectroscopy of X-ray Quasars: Searching for the X-ray Absorption from the Warm-Hot Intergalactic Medium

Taotao Fang[1,3], Claude R. Canizares[2] and Herman L. Marshall[2]

Received _____; accepted _____

[1]Department of Astronomy, University of California, Berkeley, CA 94530, fangt@astro.berkeley.edu

[2]Department of Physics and Center for Space Research, MIT, 77 Mass. Ave., Cambridge, MA 02139

[3]Chandra Fellow

ABSTRACT

We present a survey of six low to moderate redshift quasars with *Chnadra* and *XMM*-Newton. The primary goal is to search for the narrow X-ray absorption lines produced by highly ionized metals in the Warm-Hot Intergalactic Medium. All the X-ray spectra can be well fitted by a power law with neutral hydrogen absorption. Only one feature is detected at above 3-σ level in all the spectra, which is consistent with statistic fluctuation. We discuss the implications in our understanding of the baryon content of the universe. We also discuss the implication of the non-detection of the local ($z \sim 0$) X-ray absorption.

1. Introduction

Cosmological hydrodynamic simulations predict that a significant amount of baryons that reside in the Lyα forest at high redshift were shock-heated to temperatures between 10^5–10^7 K, which formed the so-called "Warm-Hot Intergalactic Medium", or WHIM (see, e.g., Hellsten et al. 1998; Cen & Ostriker 1999; Davé et al. 2000; Fang, Bryan, & Canizares 2002; Chen et al. 2003). High temperature ionized most of the neutral hydrogen, making it impossible to detect the WHIM gas in the low redshift Lyα forest. Thus,, one of the central problems in studying the baryonic content of the universe is to detect these "missing baryons".

In principal, such a component of the hot intergalactic gas can be probed via both emission and absorption. However, the diffuse nature of the hot gas make it vary hard to directly imaging the WHIM gas. On the contrary, much effect has been put in studying the absorption features produced by highly ionized metals in the spectra of background quasars.

In the past few years, significant progresses have been made in this field, thanks to

High Resolution Spectroscopy of X-ray Quasars: Searching for the X-ray Absorption from the Warm-Hot Intergalactic Medium

Taotao Fang[1,3], Claude R. Canizares[2] and Herman L. Marshall[2]

Received _____; accepted _____

[1]Department of Astronomy, University of California, Berkeley, CA 94530, fangt@astro.berkeley.edu

[2]Department of Physics and Center for Space Research, MIT, 77 Mass. Ave., Cambridge, MA 02139

[3]*Chandra* Fellow

the advancement in high resolution spectroscopy provided by the new generation of space telescopes. A significant number of O VI absorption lines have been seen with the Far Ultraviolet Spectroscopic Explorer (*FUSE*) and the Hubble Space Telescope (*HST*) (see, e.g., Savage, Tripp, & Lu 1998; Tripp, Savage, & Jenkins 2000; Tripp & Savage 2000; Simcoe, Sargent, & Rauch 2002). The distribution and derived properties of these O VI lines are consistent with predictions from simulations. In the X-ray band, Fang et al. (2002), Mathur, Weinberg, & Chen (2002), and McKernan et al. (2003) reported on the detection of intervening O VII and/or O VIII absorption lines with *Chandra* and *XMM*-Newton. Nicastro et al. (2002), Fang, Sembach, & Canizares (2003) and Rasmussen, Kahn, & Paerels (2003) also reported the detection of $z \approx 0$ X-ray absorption lines. These low redshift lines may be attributable, at least in part, to the WHIM gas in our Local Group.

Starting from *Chandra* and *XMM*-Newton observation cycle 1, we conducted a large survey of X-ray bright quasars to systematically study the potential X-ray absorption lines. In the first round, we observed two high redshift quasars (PKS 2149-306 and S5 0836+710 at $z \sim 2$, see Fang et al. 2000) and one low redshift quasar (H 1821+643 at $z \sim 0.3$, see Fang et al. 2002). In this paper, we present the results from our second round of survey, which includes a total of six *Chandra* and *XMM* targets, and a total exposure time of $\sim$ half-million seconds. These targets were selected largely based on their X-ray flux levels, which were determined by previous X-ray observations such as *Rosat* and *ASCA*. In principle, we can either take a deep look of one target, which can probe low column density absorbers, or observe several line-of-sight to increase the total pathlength. To maximize the potential information we can gain, we select the second approach.

This paper is organized as follows. We present the targets and detailed data reduction procedures in section §2. We show the continuum properties in section §3. In section §4 we discuss how we subtract continuum and do narrow line analysis. Section §5 is devoted

to detailed study of the results from narrow line analysis, and section §is summary and discussion.

2. Observation and Data Reduction

Our sample includes six quasars with redshifts ranging from $z \sim 0.13$ to ~ 0.92. Four targets (3C 279, 1ES 1028+511, 1H 0414+009, and H 1426+428) were observed with the High Energy Transmission Grating Spectrometer (HETGS, see Canizares et al. 2001) onboard the *Chandra* X-ray telescope, and two (PG 1407+265 and PKS 2135-147) were observed with the *XMM*-Newton Observatory. We list all the targets in Table 1 and their relevant observational information in Table 2. These targets were selected based on their strong X-ray flux obtained from previous *ROSAT* and/or *ASCA* observations.

2.1. *Chandra* Data Analysis

The *Chandra* HETGS produces a zeroth order image at the aim-point on the focal plane detector, the ACIS-S array, with higher order spectra dispersed to either side (for ACIS-S, see Garmire et al. 2001). For all four *Chandra* observations, the telescope pointing direction was offset 20″ along +Y in order to move the zeroth order off a detector node boundary, and the Science Instrument Module (SIM) was moved toward the read-out row by about 3 *mm* to get better ACIS energy resolution (for detailed instrument setups, see the *Chandra* Proposers' Observatory Guide, or POG[4]). Figure 1a, b, c, and d display the zeroth-order images. We also label a size of 5″ in each panel. 1H 0414+009, 1ES 1028+511, and H 1426+428 appear to be point sources with core sizes less than 2 – 3 ″; however, a

[4]See *Chandra* Proposers' Observatory Guild (POG) at http://asc.harvard.edu.

large scale jet is clearly presented in the zeroth order image of 3C 279 (south-east direction). Detailed study of this X-ray jet will be presented in a separate paper (Marshall, Cheung, Canizares, & Fang 2003).

Chandra data were analyzed with the standard pipeline for the *Chandra* HETGS provided by the Chandra X-ray Center (CXC)[5]. We use *Chandra* Interactive Analysis of Observations (CIAO) V3.0. The standard screening criteria were applied to the data. We selected photon events with *ASCA* grades 0, 2, 3, 4, 6 and excluded those with energies above 10 keV. We also removed hot columns and bad pixels in each CCD chip. The HETGS consists of two different grating assemblies, the High Energy Grating (HEG) and the Medium Energy Grating (MEG), and provides nearly constant spectral resolution ($\Delta\lambda = 0.012\mathring{A}$ for HEG and $\Delta\lambda = 0.023\mathring{A}$ for MEG) through the entire bandpass (HEG: 0.8-10 keV, MEG: 0.4-8 keV). The moderate energy resolution of the CCD detector ACIS-S is used to separate the overlapping orders of the dispersed spectrum. We added the plus and minus sides to obtain the first order spectra of both grating assemblies. In cases where two observations were performed for one target (1H 0414+009 and 1ES 1028+511), we use CIAO tool "add_grating_spectra" to add two spectra together, and average the auxiliary response files (ARF).

2.2. *XMM*-Newton Data Analysis

We obtained data for PG 1407+265 and PKS 2135-147 with all the instruments onboard *XMM*-Newton, and here we focus on EPIC (including MOS1, MOS2 and PN) and RGS (including RGS1 and RGS2) data. While with high spectral resolution RGS data will be analyzed to study narrow line features, we also study EPIC data to obtain the

[5]See http://asc.harvard.edu/

information regarding QSO continuum. Figure 1e and f shows the MOS images of both QSOs.

All the EPIC observations were performed with the "`PrimeFullWindow`" and "`Imaging`" data mode. A medium filter was applied. Data were processed with the standard software, *XMM*-Newton Science Analysis System (SAS) V5.4 [6]. We applied the standard SAS tasks "`emchain`" and "`epchain`" to obtain event files for MOS and PN data, respectively. We selected events with patterns between 0 and 12 for MOS and those with patterns between 0 and 4 for PN. All events within central region with a radius of 30″ were extracted for the point source spectra and areas between 30″ and 60″ for the background spectra. We also checked the pile-up level with the SAS task "`epatploy`" and found that there is no significant pile-up between 0.4 and 10 keV, so we chose this energy range for the subsequent spectral fitting. Finally, all the spectra were binned to have a minimum of 20 counts per bin.

RGS 1 and 2 spectra were extracted using "`rgsproc`". This SAS task also provided a combined RMF and ARF file for each spectrum. To achieve the highest signal-to-noise, we added both RGS (including the first and second order spectra) together. The combined spectrum was then grouped channel by channel to have a constant bin size of 0.025 $\AA$, half of the width of the RGS FWHM, for the subsequent narrow line analysis.

---

[6]see http://xmm.vilspa.esa.es/

Table 1: Target Parameters

Target	RA (J2000)	Dec (J2000)	Redshift	N_H (10^{20}cm^2)
PG 1407+265	14 09 23.9	26 18 21	0.940	1.38
PKS 2135-147	21 37 45.2	-14 32 55	0.200	4.77
1H 0414+009	04 16 52.4	01 05 24	0.287	9.15
1ES 1028+511	10 31 18.4	50 53 36	0.361	1.27
3C 279	12 56 11.1	-05 47 22	0.536	2.21
H 1426+428	14 28 32.6	42 40 21	0.129	1.36

Table 2: Observation Log

Target	Telescope	Observation ID	Observation Date	Duration (sec)
PG 1407+265	*XMM*	0092850501	2001-12-22	42,062
PKS 2135-147	*XMM*	0092850201	2001-04-29	59,850
1H 0414+009	*Chandra* HETGS	2969	2002-08-01	52,000
		4284	2002-08-02	41,000
1ES 1028+511	*Chandra* HETGS	2970	2002-03-27	25,000
		3472	2002-03-28	75,000
3C 279	*Chandra* HETGS	2971	2002-03-21	107,000
H 1426+428	*Chandra* HETGS	3568	2003-09-08	102,000

3. Continuum Properties of Individual Source

Continuum can be fitted by a power law with absorption from neutral hydrogen. The flux $F(E)$ can be expressed as

$$F(E) = A_{pl}\left(\frac{E}{1\,\mathrm{keV}}\right)^{-\Gamma}\exp\left[-\sigma(E)N_H\right]. \quad (1)$$

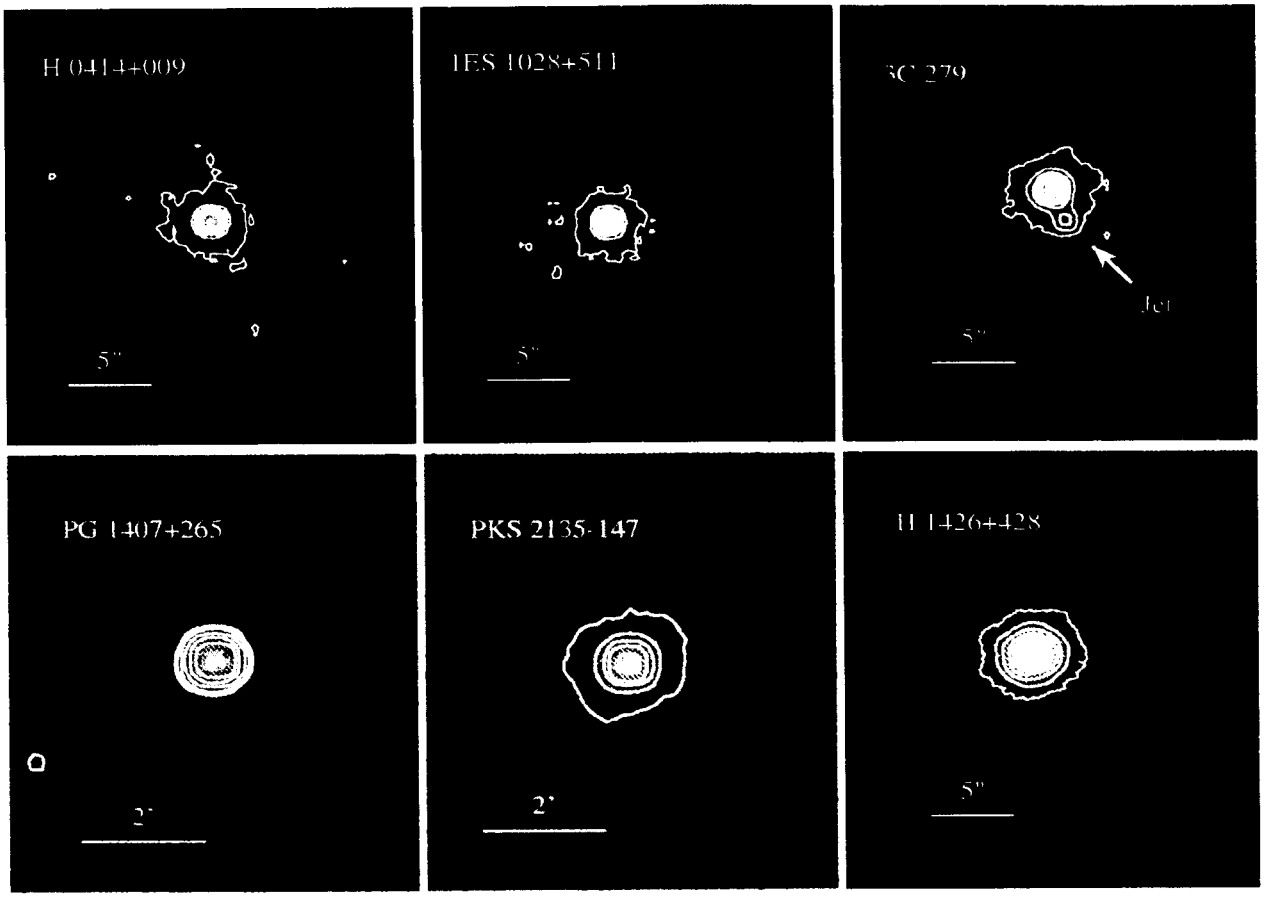

Fig. 1.— X-ray images of all the targets. The white line in the bottom of each panel shows the angular size. For the 4 *Chandra* targets, the zeroth order images are shown here; and EPIC images are shown for the two *XMM*-Newton targets.

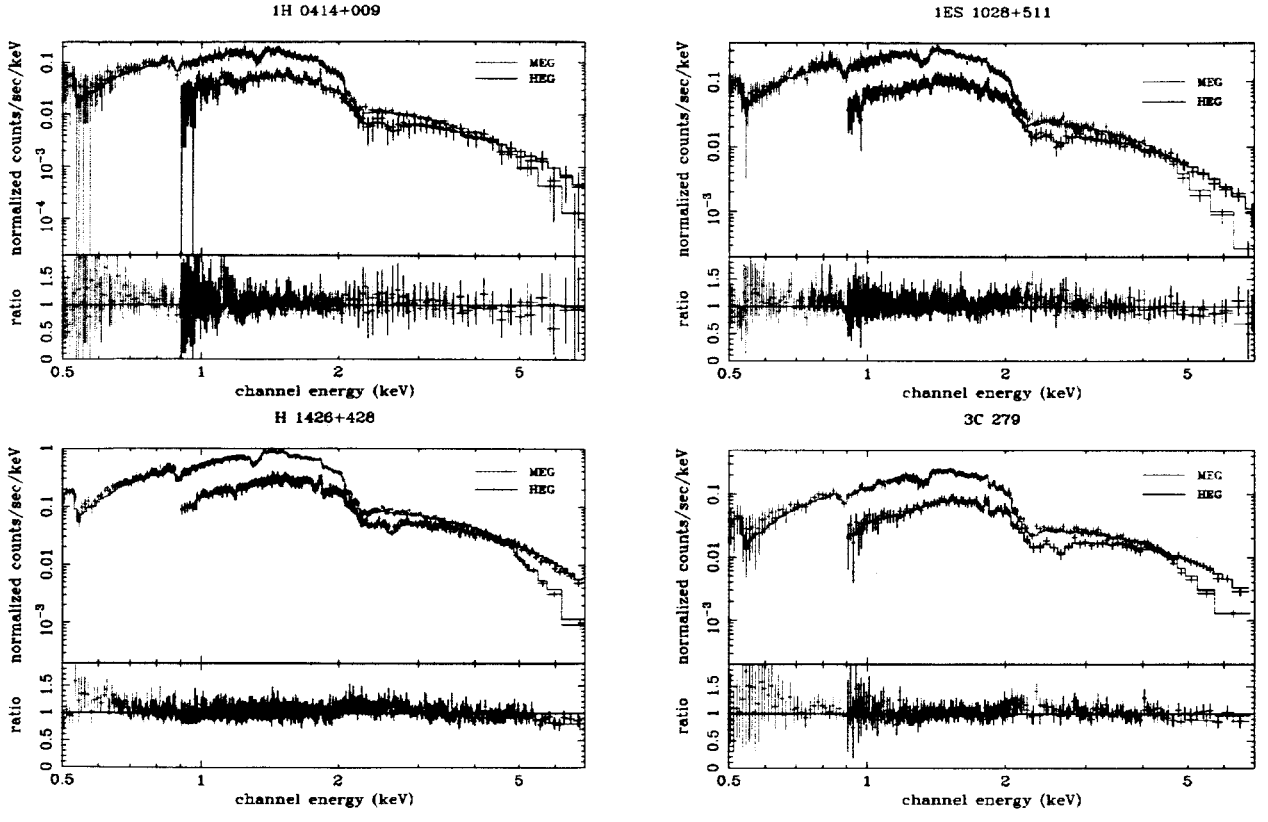

Fig. 2.— *Chandra* MEG (red line) and HEG (dark line) spectra. Solid lines in each plot represent the best fitted models. The bottom panel of each plot shows the ratio between data and model.

Here A_{pl} is the normalization at 1 keV, Γ is the photon index, E is the photon energy, $\sigma(E)$ is the photoionization cross section, and N_H is the neutral hydrogen column density. Table 3 lists the fitting parameters for all the targets and inferred fluxes and luminosities. Fitting was performed with XSPEC V11.3 [7]. For each *Chandra* data set we fit with with two models: (a) a power law with a fixed neutral hydrogen absorption at the Galactic level, and (b) a power law with a variable hydrogen absorption, and we fit both HEG and MEG data simultaneously. In the top four targets in Table 3, the first rows show the fitted results from model (a) and the second rows show results from model (b). For the two *XMM* targets, since we cannot constrain the hydrogen column density (N_H), we fix them at the Galactic value and fit the data with model (a) only. The fit was performed with all the three instruments (MOS1, MOS2 and PN) simultaneously. We emphasize that while some spectra show complex continuum structures and may require additional components, for the purpose of searching the narrow absorption features, we stick to the simplest single power law model, and leave detailed spectral studies to a future paper.

---

[7]see http://heasarc.gsfc.nasa.gov/docs/xanadu/xspec/

Table 3: Spectral Fitting Parameters

Target	N_H ($10^{20}\,cm^2$)	Photon Index (Γ)	$A_{pl}{}^a$	$f_{2-10}{}^b$	$L_{2-10}{}^c$	χ^2/dof
3C 279	...	1.51 ± 0.02^d	2.96 ± 0.04	1.4	1.5×10^{46}	382/950
	7.4 ± 2.2	1.59 ± 0.04	$3.25^{+0.14}_{-0.13}$	1.3	1.5×10^{46}	365/949
H 1426+428	...	1.81 ± 0.01	11.87 ± 0.09	3.6	1.7×10^{45}	1126/950
	11.0 ± 0.9	1.99 ± 0.02	14.50 ± 0.28	3.4	1.6×10^{45}	748/949
1H 0414+009	...	2.47 ± 0.05	3.25 ± 0.08	0.4	1.2×10^{45}	263/950
	$13.40^{+3.26}_{-3.08}$	2.57 ± 0.09	$3.56^{+0.27}_{-0.24}$	0.4	1.2×10^{45}	258/949
1ES 1028+511	...	2.11 ± 0.02	4.77 ± 0.07	1.0	4.5×10^{45}	399/950
	$6.69^{+1.76}_{-1.70}$	2.23 ± 0.04	5.38 ± 0.22	0.9	4.6×10^{45}	258/949
PG 1407+265	...	$2.27^{+0.01}_{-0.02}$	0.43 ± 0.01	0.08	4.0×10^{45}	826/774
PKS 2135-147	...	1.84 ± 0.01	1.62 ± 0.01	0.5	5.9×10^{44}	2161/1521

a. Flux at 1 keV (observer's frame) in units of 10^{-3} photons $cm^{-1}s^{-1}keV^{-1}$.

b. Flux between 2 — 10 keV (observer's frame), in units of 10^{-11} ergs $cm^{-2}s^{-1}$.

c. Intrinsic luminosity between 2 — 10 keV, in units of ergs s^{-1}.

d. Errors are quoted as 90% confidence.

Comments on individual source:

- *3C 279*: This source is a radio loud quasar (RLQ) and was identified as the first superluminal source (Whitney et al. 1971). Our *Chandra* observation, for the first time, revealed the jet in X-ray band (for detail see Marshall, Cheung, Canizares, & Fang 2003). While both *Rosat* (Comastri, Fossati, Ghisellini, & Molendi 1997; Sambruna 1997) and *ASCA* (Reeves & Turner 2000) observations showed similar photon indices ($\Gamma \sim 1.8$), we obtained a relatively flat spectrum with *Chandra* ($\Gamma \sim 1.5 - 1.6$). The fluxes and luminosities are consistent among these observations.

- *H 1426+428*: This is a BL Lac object and was extensively observed with *HEAO-1* (Wood et al. 1984), *EXOSAT* (Remillard et al. 1989), *BBXRT* (Madejski et al. 1992), *ROSAT* and *ASCA* (see,e.g.,Sambruna et al. 1997), and *BeppoSAX* (Costamante et al. 2001). Our result shows that the fitted N_H is significantly higher than the Galactic value, which is consistent with results from *BBXRT* and *ASCA* but not with *ROSAT* (Sambruna et al. 1997). The observed flux between 2 — 10 keV varied from ~ 2 to $\sim 5 \times 10^{-11}\,\mathrm{ergs\,cm^{-2}s^{-1}}$ among various observations, while the photon index varies slightly around 2. While *BBXRT* reported an X-ray absorption feature at ~ 0.66 keV (Madejski et al. 1992; Sambruna et al. 1997), we could not confirm this in our *Chandra* MEG spectrum, consistent with results from recent *XMM*-Newton observations (Blustin, Page, & Branduardi-Raymont 2003).

- *H 0414+009*: This target is a BL Lac object associated with a galaxy cluster of Abell richness of 0 (Falomo, Pesce, & Treves 1993). *BeppoSAX* and *ROSAT* observations (Wolter et al. 1998) showed similar photon indices. However, we obtain a lower 2 — 10 keV flux, indicating flux variation by a factor of ~ 2. We also find a slightly high N_H, compared with the Galactic value.

- *1ES 1028+511*: The redshift of this BL Lac object has been accurately determined as $z = 0.361$, based on the measurement of two Ca II absorption lines (Polomski et al. 1997). *Rosat* observation showed a power law spectrum with $\Gamma = 2.43 \pm 0.20$ and an unabsorbed flux of $6.16 \times 10^{-11}\,\mathrm{ergs\,cm^{-2}s^{-1}}$ between 0.5 — 2.4 keV. This source was also among sources that listed in the *ASCA* Medium Sensitive Survey (Ueda et al. 2001) with a flux of $7.77 \times 10^{-12}\,\mathrm{ergs\,cm^{-2}s^{-1}}$ between 2 — 10 keV, assuming a photon index of 1.7.

- *PG 1407+265* It's one of the brightest quasars at redshift around 1. There is weak evidence for Damped Lyα Absorption and for Laman Limit System. in its optical

continuum (Lanzetta, Wolfe, & Turnshek 1995). *HST* observation revealed intrinsic narrow absorption features of O VI and Lyα in the quasar rest frame (Ganguly et al. 2001). Previous *ASCA* observation showed a spectrum with similar photon index ($\Gamma \sim 2$) but stronger 2 — 10 keV flux (Reeves & Turner 2000).

- *PKS 2135-147*: This is a typical double-lobe, radio source (Miley & Hartsuijker 1978; Gower & Hutchings 1984). X-ray observations with *Einstein* (Wilkes & Elvis 1987) and *EXOSAT* (Singh, Rao, & Vahia 1991) reported a photon index consistent with our observation; however, *Rosat* observations (Rachen, Mannheim, & Biermann 1996) showed a much steeper spectrum, with $\Gamma \sim 2.5$. We also obtained a lower X-ray flux, compared with previous observations. Optical and UV spectra show strong absorption lines of O VI, N V and Lyα at $z_{abs} \sim z_{em}$ (Hamann et al. 1997). These lines also lie near the center of a small cluster and is very close to three galaxies inside that cluster. It is still unclear whether these absorption lines are intrinsic or due to the intervening systems.

4. Narrow Line Analysis

Cosmological simulations predict that typical X-ray absorption lines from the WHIM gas have line width in the order of mÅ (see, e.g., Hellsten, Gnedin, & Miralda-Escudé 1998; Fang, Bryan, & Canizares 2002; Chen, Weinberg, Katz, & Davé 2003). On the observation side, the detection of such narrow features relies on a careful measurement of the continuum level. Using 1ES 1028+511 as an example, in Figure 4 we show how we obtain a continuum-subtracted spectrum.

Figure 4 shows a small portion of the raw count spectrum of 1ES 1028+511 plotted against wavelength. The solid dark line in the top panel shows the MEG first order counts

between 5 and 7 Å, with a bin size of 0.01Å. The bin size is chose in such a way that there are two bins across the point spread function (PSF) of the instrument. In this way the bin size is 0.005Å for *Chandra* HEG, 0.01Å for MEG and 0.025Å for *XMM* RGS [8]. The red line (labeled model 1) shows the continuum from a power law plus neutral hydrogen absorption, with the fitting parameters adopted from Table 3. The bottom panel gives χ, which is defined as:

$$\chi \equiv \frac{C_d - C_m}{\sqrt{C_m}}, \tag{2}$$

where C_d is the data count per bin and C_m is the corresponded model count in that bin.

While in general such a model provides a good fit to the overall spectrum, in some local regions it will either over or under-estimate the observed counts due to systematic and/or statistic fluctuations. Clearly, in the bottom panel of Figure 4, there are more red bins above zero than bins below zero, which means in the 5 – 7Å region, model 1 underestimates the count. To eliminate this problem, we adopt an optimized local fitting technique: the whole spectrum was divided into several small regions; in each region we fit the continuum with a polynomial — the fit was tested with polynomials of orders between 1 and 10, and the one that gave the minimum χ^2 was selected. To avoid significant deviation caused by one or two randomly high or low χ bins, we ignore all the bins with $|\chi| > 3$ before fitting. This method allows us to minimize the fluctuations at large scales, and still preserve features with width narrower than several hundred mÅ. We find the histogram distribution of the χ obtained in this method can be well fitted by a Gaussian distribution. We call this method "model 2" and plot it in blue in Figure 4. Clearly, model 2 provides a significantly better fit.

---

[8]See http://asc.harvard.edu/proposer/POG/html/HETG.html and http://xmm.vilspa.esa.es/external/xmm_user_support/documentation/uhb/node45.html for the width of instrument PSF of *Chandra* HETG and *XMM* RGS, respectively.

The next step is to identify any potential absorption (or emission) features in the spectrum. Our search criterion is still based on χ: we search for any feature which has at least two continuous bins with $|\chi| > \chi_{min}$. Assuming the signal-to-noise ratio (SNR) in the first bin is χ_1 and in the next bin is χ_2, The total SNR in these two bins follows $\chi = (\chi_1 + \chi_2)/\sqrt{2}$. To ensure a minimum detection of at least 3σ, we need to have both $|\chi_1|$ and $|\chi_2| \gtrsim 2$. To be conservative, we set $\chi_{min} = 1.5$. We label features identified with this requirement as potential absorption or emission lines. We then fit the continuum-subtracted residual with a Gaussian line profile around the features we identified. The subtraction and fitting are performed with the software package ISIS (Interactive Spectral Interpretation System, see Houck & Denicola 2000) [9]

Combining all the data together, we have a total of $\sim$ 13,000 bins. To enhance the detection, we select bins which have at least 15 counts. This leaves us $\sim$ 4,500 bins. Based on the above criteria, we find a total of 23 possible absorption features. Other stringent criteria are enforced to eliminate false detections, including that a true feature should appear in both MEG and HEG spectra for *Chandra* targets, and that we should avoid regions right at the instrument features - these regions typically show large discrepancies between model and data. With these criteria we found only one feature, which is located on the MEG spectrum of H 1426+426 at 20.41 $\AA$ with a SNR of 3.3. How many such features can be caused by random fluctuation? We ran a set of Monte-Carlo simulations to see how many features can be generate from a Poisson fluctuation. We find that the number is $\sim$ 17 for $\sim$ 4,500 bins, and the expected line number with a SNR $\gtrsim$ 3.3 is $\sim$ 0.2. So in conclusion we find the total features we detected are roughly consistent with pure Poisson fluctuations. We also searched for emission features and find no significant detections.

---

[9]see http://space.mit.edu/ASC/ISIS/

5. Discussion

5.1. Intervening IGM Absorption

Based on the non-detection of any significant absorption features, we can determine the minimum detectable ion column densities at a certain SNR level. Given the quasar continuum flux f_X, the minimum detectable line equivalent width (W_λ) is

$$W_\lambda = SNR \times \left(\frac{\lambda}{f_X RAT}\right)^{\frac{1}{2}}, \tag{3}$$

where λ is wavelength, $R \equiv \lambda/\Delta\lambda$ is the resolving power, A is the effective area and T is the exposure time. We expect weak, unresolved features from the linear part of the curve-of-growth. The minimum detectable column density (N_i) and equivalent width W_λ then follow the linear relationship (Spitzer 1978)

$$\frac{W_\lambda}{\lambda} = 8.51 \times 10^{-13} N_i \lambda f. \tag{4}$$

Here f is the oscillator strength.

In Table 4 we list the minimum detectable column densities of O VII and O VIII along the line-of-sight towards these six targets. We adopt a SNR of 3 here. The rest frame wavelengths of O VII and O VIII are 21.6019 Åand 18.9689 Å, respectively (Verner & Yakovlev 1995) . Since *Chandra* HEG has no effective area in the longer wavelength of both transitions, we use MEG only for the four *Chandra* targets. Since MEG has no effective area above 25 – 26 Å, we can probe the line detection upto $z \sim max(z_i, 0.35)$ for O VIII and $z \sim max(z_i, 0.2)$ for O VII, where z_i is the redshift of individual sources.

Table 4: Limits on Column Density [a]

Target	O VIII	O VII
1H 0414+009	1.87	1.12
1ES 1028+511	1.44	0.86
H 1426+428	1.00	0.60
3C 279	1.87	1.12
PG 1407+265	2.29	1.37
PKS 2135-147	2.36	1.02

a. All column densities are in units of $10^{16}\,\mathrm{cm}^{-2}$.

Using standard cosmological models and ingredients from galaxy and large scale structure evolution, numerical simulations predict the spatial distribution of metals and their ionization structures (see, e.g., Cen & Ostriker 1999). Such simulations allow us to make quantitative predictions of the absorption features that could be present in the spectra of background sources (see, e.g., Hellsten, Gnedin, & Miralda-Escudé 1998; Fang, Bryan, & Canizares 2002; Chen, Weinberg, Katz, & Davé 2003). Our non-detection of any significant absorption lines can, convensely, put constraints on cosmological parameters and other physical processes adopted in the simulations.

Rather than running complicated hydrodynamic simulations with various cosmological parameters and physical processes to explore the parameter space that can be constrained by our observation results, we adopted a simple but effective analytic approach that follows Perna & Loeb (1998), Fang & Canizares (2000). The basic idea is that all the hot gas is distributed within virialized halos that follow a Press-Schechter distribution (Press & Schechter 1974). Given a certain density profile of a virialized halo, the probability that a random line-of-sight that passes through a halo of mass M with an impact parameter b can be calculated. Based on assumptions of metal abundance, we can then calculate

the so-called "X-ray Forest Distribution Function" (XFDF), defined as $\partial^2 P/(\partial N_i \partial z)$, the absorption line number per unit redshift (z) per column density (N_i) for ion species i. Specifically, XFDF can be analytically calculated as

$$\frac{\partial^2 P}{\partial N_i \partial z} = \int_M \frac{dn}{dM} \frac{d\Sigma}{dN_i} \frac{dl}{dz}, \tag{5}$$

where (dn/dM) is the distribution of the comoving virialized halo, Σ is the cross section of the halo, and l is the path length.

How accurate this analytic approach is? Fang, Bryan, & Canizares (2002) compared both numerical and semi-analytic methods (with the above analytic model and a halo temperature profile fitted from simulation). For O VII and O VIII, it turns out that there is large discrepancy in the low column density region ($N_i \sim 10^{12} - 10^{15}\,\mathrm{cm}^{-2}$), where most lines are distributed in the filamentary structures seen in the numerical simulations but which cannot be described by Press-Schechter formalism. At the high column density end ($N_i \gtrsim 10^{15}\,\mathrm{cm}^{-2}$), the semi-analytic method provides a reasonablely good fit to results from numerical simulations. These high column density lines distribute typically in virialized halos with higher temperatures and densities thsn found in the filaments. Since in our study the minimum detectable column densities are around $10^{16}\,\mathrm{cm}^{-2}$, we can apply the analytic approach in the following study.

Given the XFDF and certain cosmological parameters, we can calculate the expected absorption line number by combining observations on all the six targets. The total absorption line number is then

$$n = \sum_j \int_{N_i(j)}^{\infty} \int_0^{z_j} \frac{\partial^2 P}{\partial N_i \partial z} dN_i dz. \tag{6}$$

Here $N_i(j)$ is the minimum detectable column density of ion i for the jth target; z_j is its maximum redshift that can probed with the *Chandra* and *XMM*-Newton instruments; and overall summation is over all the six targets (index j).

The parameters we plan to constrain are the cosmic matter density Ω_m and metal abundance Z (in units of the solar abundance $Z_\odot$.) Changes in these two parameters will dramatically change gas and metal content and could have significantly impact on the detectability of X-ray absorption lines. We keep all the other parameters at the standard values: we use the ΛCDM model with a dark energy density of $\Omega_\Lambda = 1 - \Omega_m$, the hubble constant is $H_0 = 100h\,\mathrm{km\,s^{-1}Mpc^{-1}}$ with $h = 0.67$; the baryon density is $\Omega_b = 0.04$; and we assume the gas fraction is $f_{gas} = 0.2$.

Figure 11 shows the expected total O VII (black lines) and O VIII (red lines) line numbers with different Ω_m and metal abundance Z. Since we detect no absorption line, the horizontal green line show the 1-σ upper limit (Gehrels 1986). The vertical green line shows the value of Ω_m measured with *WMAP* (Spergel et al. 2003). The green arrows indicate allowed regions. Clearly, for O VIII, even when we use $Z = 0.3Z_\odot$ (the red dashed line), the best constraint we have is $\Omega \lesssim 0.6$, far more than the value measured by *WMAP*. O VII provides much better constraints. For instance, if $Z = 0.2Z_\odot$, the matter density should be $\Omega_m \lesssim 0.25$. On the other hand, if we adopt the *WMAP* value of Ω_m, the metal abundance should be smaller than 0.1 - 0.2 $Z_\odot$.

5.2. Local ($z \approx 0$) Absorption

Recently, there are a number of cases showing local ($z \approx 0$) X-ray absorption lines along several line-of-sight. These background quasars, namely, 3C 273, PKS 2155-304, Mkn 421 and NGC 3783 (see, Kaspi et al. 2002; Nicastro et al. 2002; Fang, Sembach, & Canizares 2003; Rasmussen et al. 2003; Cagnoni et al. 2004), are among the brightest extragalactic X-ray sources in the sky and some of them were used as calibration targets. In Figure 12 we show the (l, b) coordinates of these targets (in blue). The high column densities of these X-ray absorbers ($N \sim 10^{15} - 10^{16}\,\mathrm{cm^{-2}}$) imply the existence of large amount of hot

gas. Given the current instrument resolution with *Chandra* and *XMM*-Newton, it is still unclear where this hot gas locate: in the interstellar medium, in the distant halo, or in the Local Group as the intragroup medium.

We also show the positions of the six targets in this paper (in red). Most of these targets locate at positions with high latitude, with small Galactic neutral hydrogen absorption. Due to the low fluxes, we do not find any local absorption features in all the six targets. To test whether there is a universal hot gas around our Galaxy, we stack several data sets together to search for local absorption lines. Here we select only *Chandra* observations to avoid complicate issues like the calibration of absolute wavelength between different X-ray telescopes. No absorption line were detected in the stacked data. However, given the larger signal we got, we found the 3-σ limit of the minimum detectable equivalent width is 17.1 mÅ for O VII and 11.6 mÅ for O VIII. These correspond to column densities of $\sim 5.9 \times 10^{15}\,\mathrm{cm}^{-2}$ for O VII and $\sim 8.7 \times 10^{15}\,\mathrm{cm}^{-2}$ for O VIII, respectively. These limits are comparable to (and a little lower than) limits we got from H 1426+428. It is easy to understand: H 1426+428 is the brightest among all the quasars observed in our sample, which dominates the estimation of the equivalent width.

In summary, although several local X-ray absorption lines have been observed with *Chandra* and *XMM*-Newton, our data suggests that there is no universal X-ray hot gas surround us, at least with O VII and/or O VIII column densities of over $10^{16}\,\mathrm{cm}^{-2}$.

6. Summary

In this paper we present our *Chandra* and *XMM*-Newton observations of six quasars, with redshifts ranging from ~ 0.1 to ~ 0.9. Our main conclusions can be summarized as follows.

1. We obtained the continuum information of these six targets. All of them can be fitted quite well with a power law with absorption from neutral hydrogen, although some of these targets may require complicated model(s) to achieve a better fit.

2. Our main purpose is to search for any narrow absorption features in the X-ray spectra that were produced by the WHIM gas. After applying an optimized local fitting technique to subtract continuum, we found a total of 23 narrow features at or above 3σ lever. A cross check with instrument features excludes most features, leaving only one with a SNR $\gtrsim 3.3$, which is consistent with random fluctuation. Thus we conclude that no absorption feature was detected in our observations.

3. Given the large sample of our survey, we are able to put much stronger constraints on cosmological parameters, comparing with previous studies (see, e.g., Fang & Canizares 2000). Assuming a simple halo model for X-ray absorber, we found $\Omega_m \lesssim 0.25$ if we adopted a halo metal abundance of $0.2Z_\odot$, or the metal abundance should be smaller than 0.1 - 0.2 $Z_\odot$ if we adopted a *WMAP* value of Ω_m.

4. We also search any local ($z \sim 0$) absorption lines, which have been detected in several other cases. No local absorption line was found. By stacking the data together, we are able to reach minimum detectable column densities as low as $(5.9, 8.7) \times 10^{-15}\,\mathrm{cm}^{-2}$ for (O VII, O VIII), respectively.

Though several line of evidences implied the existence of the WHIM gas, a firm prove of such "missing baryons" still remains an important challenge in cosmology. Future X-ray missions are very promising in detecting WHIM gas (see, e.g., Chen, Weinberg, Katz, & Davé 2003). Both *Constellation*-X and *XEUS* can probe highly ionized metals to column densities of as low as 10^{14} - $10^{15}\,\mathrm{cm}^{-2}$. Such high resolution and sensitivities will reveal a true "X-ray Forest" in the IGM. By comparing observations with numerical simulations

and analytic analysis, we may eventually obtain a complete theory of structure formation and evolution from the big bang to the present epoch.

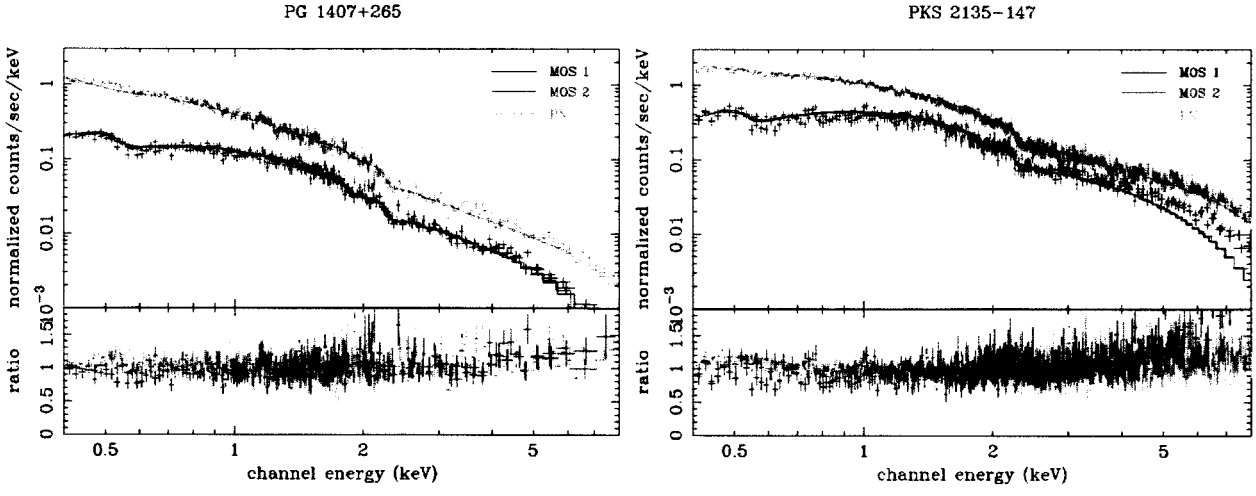

Fig. 3.— *XMM*-Newton MOS1 (dark), MOS2 (red), and PN (green) spectra. Solid lines in each plot represent the best fitted models. The bottom panel of each plot shows the ratio between data and model.

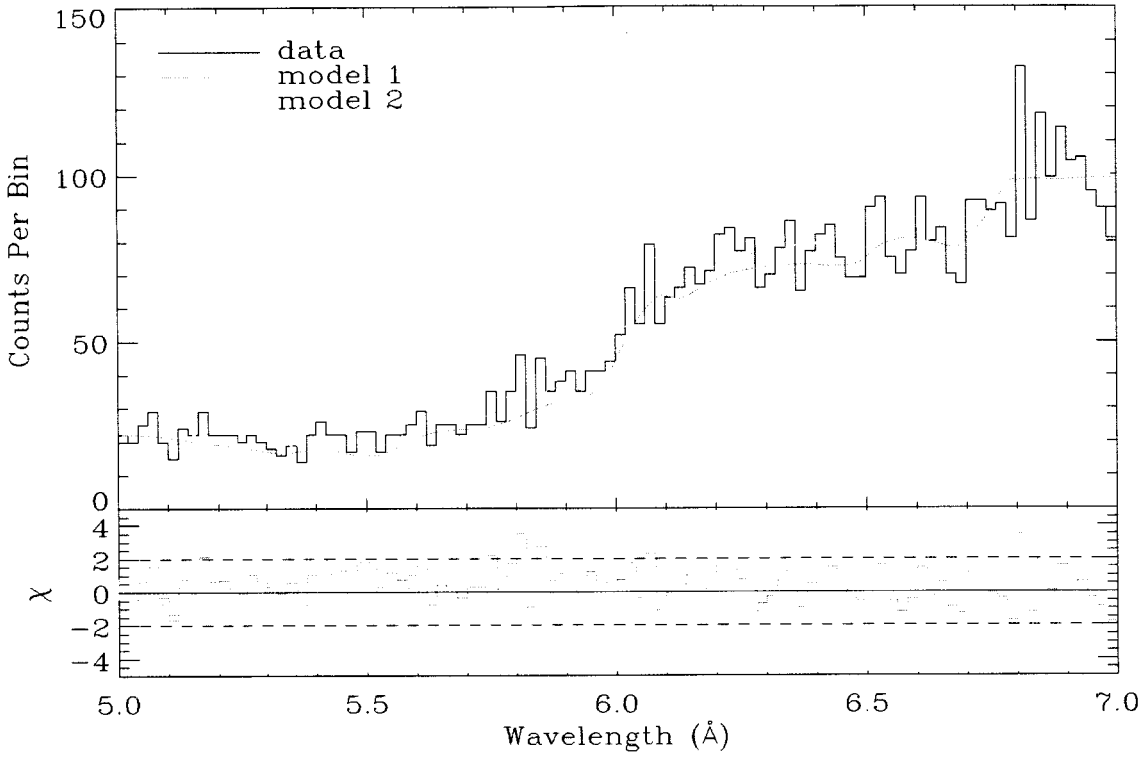

Fig. 4.— A sample of data (dark) and comparison between two models. Model 1 (shown in red) adopted simplily the best fitted model from Table 3, and model 2 (blue) uses an optimal local fitting technique. Bottom panel shows the χ of each model. Clearly, model 2 is a better fit to data.

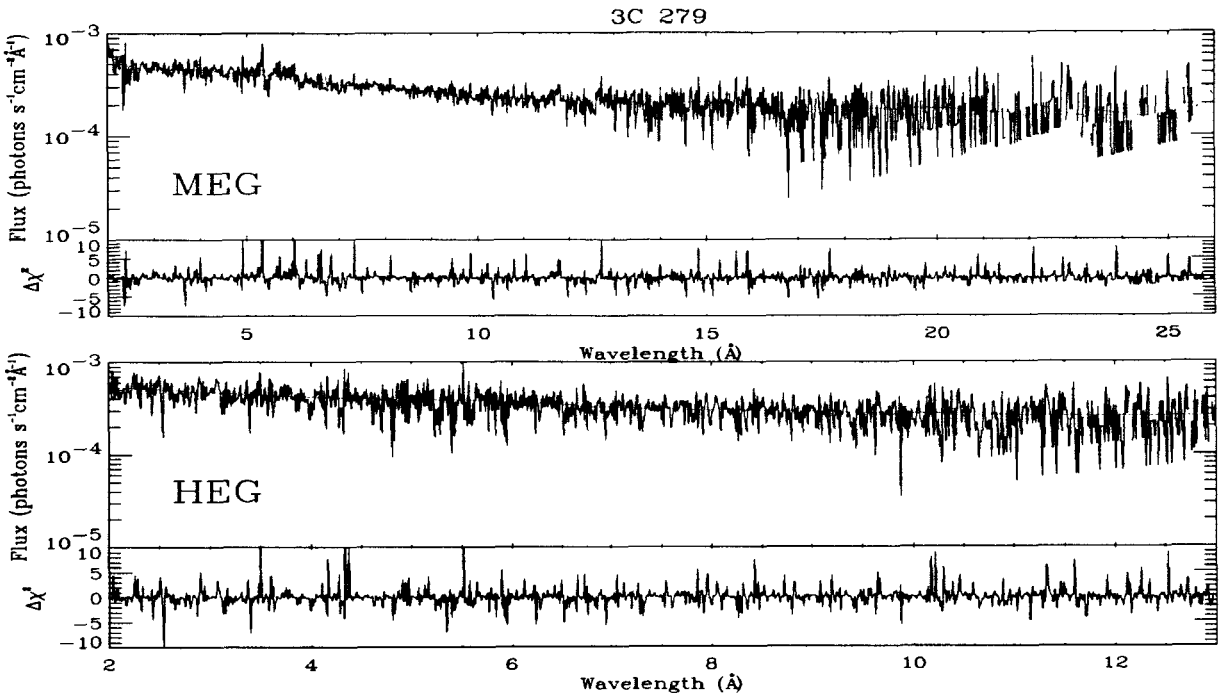

Fig. 5.— *Chandra* MEG (top panel) and HEG (bottom panel) spectra of 3C 279. Red lines show best fitted spectra from model 2. The bottom of each panel show the $\Delta\chi^2$.

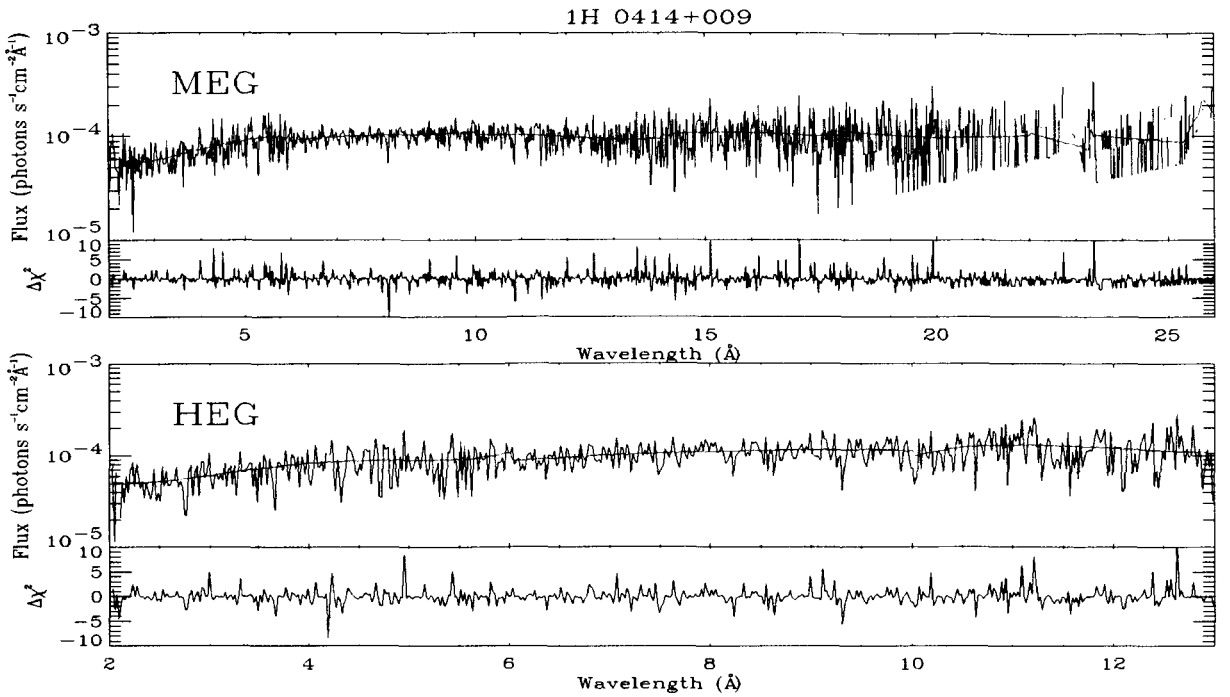

Fig. 6.— Same as Figure 5 but for 1H 0414+009.

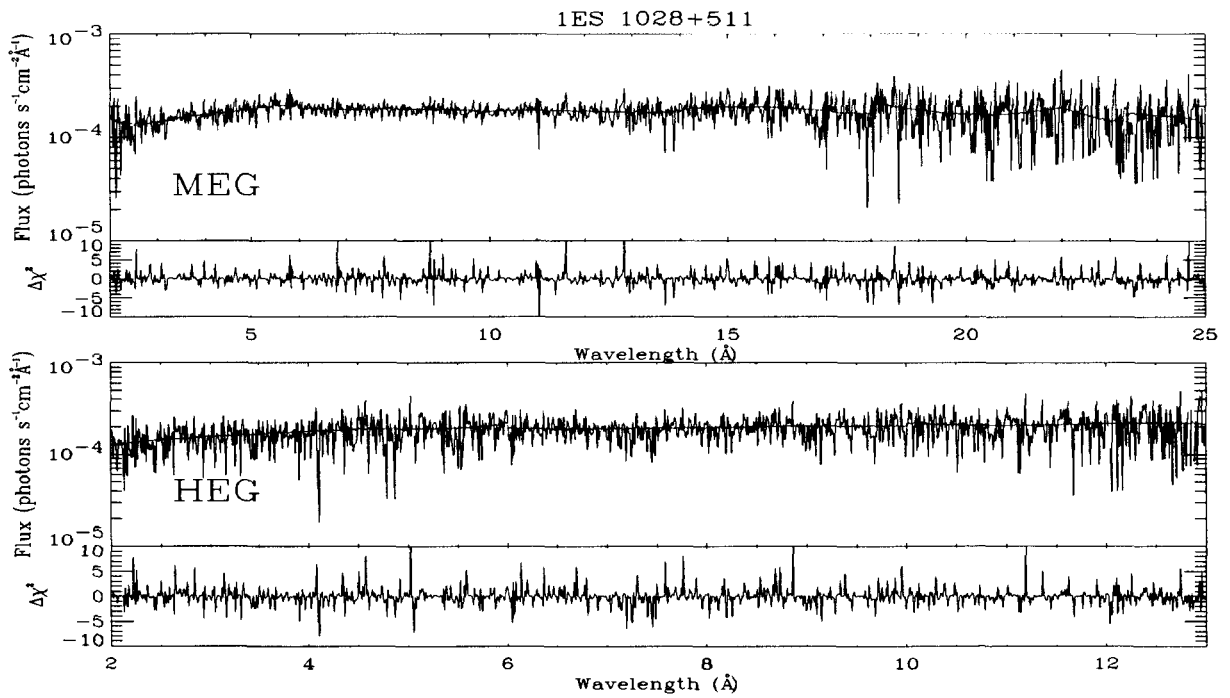

Fig. 7.— Same as Figure 5 but for 1ES 1028+511.

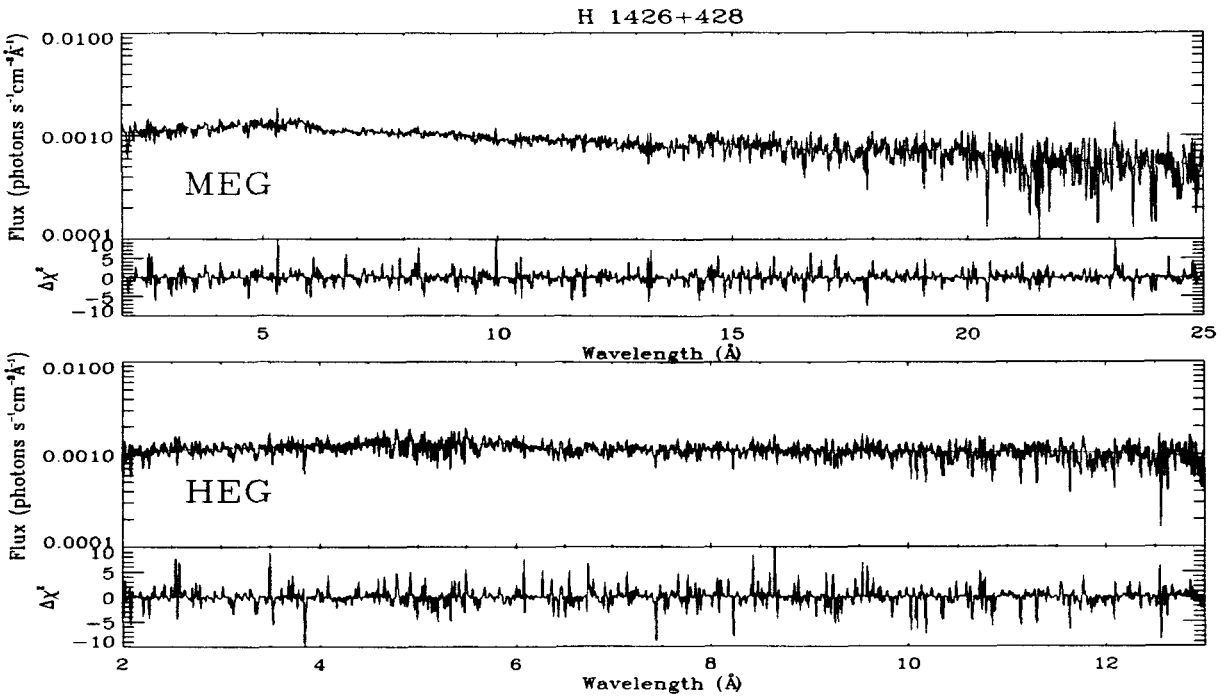

Fig. 8.— Same as Figure 5 but for H 1426+428.

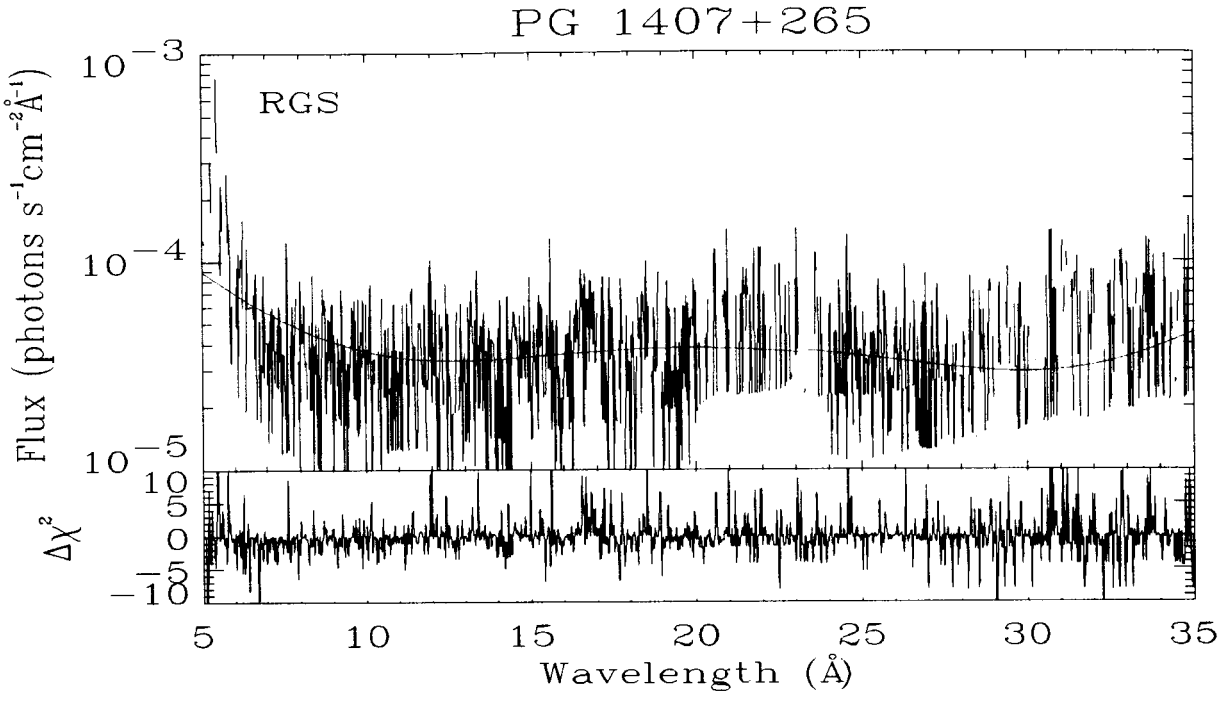

Fig. 9.— *XMM*-Newton RGS spectrum of PG 1407+265. Lines are the same as those in Figure 5.

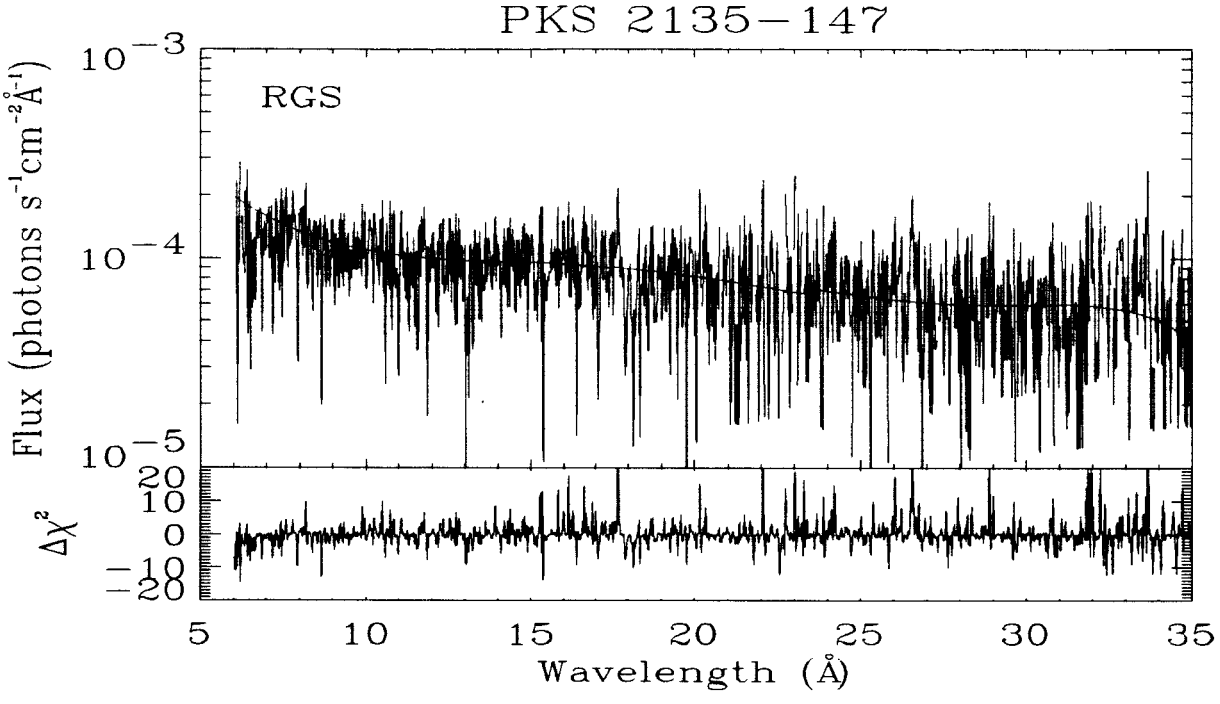

Fig. 10.— *XMM*-Newton RGS spectrum of PKS 2135-147. Lines are the same as those in Figure 5.

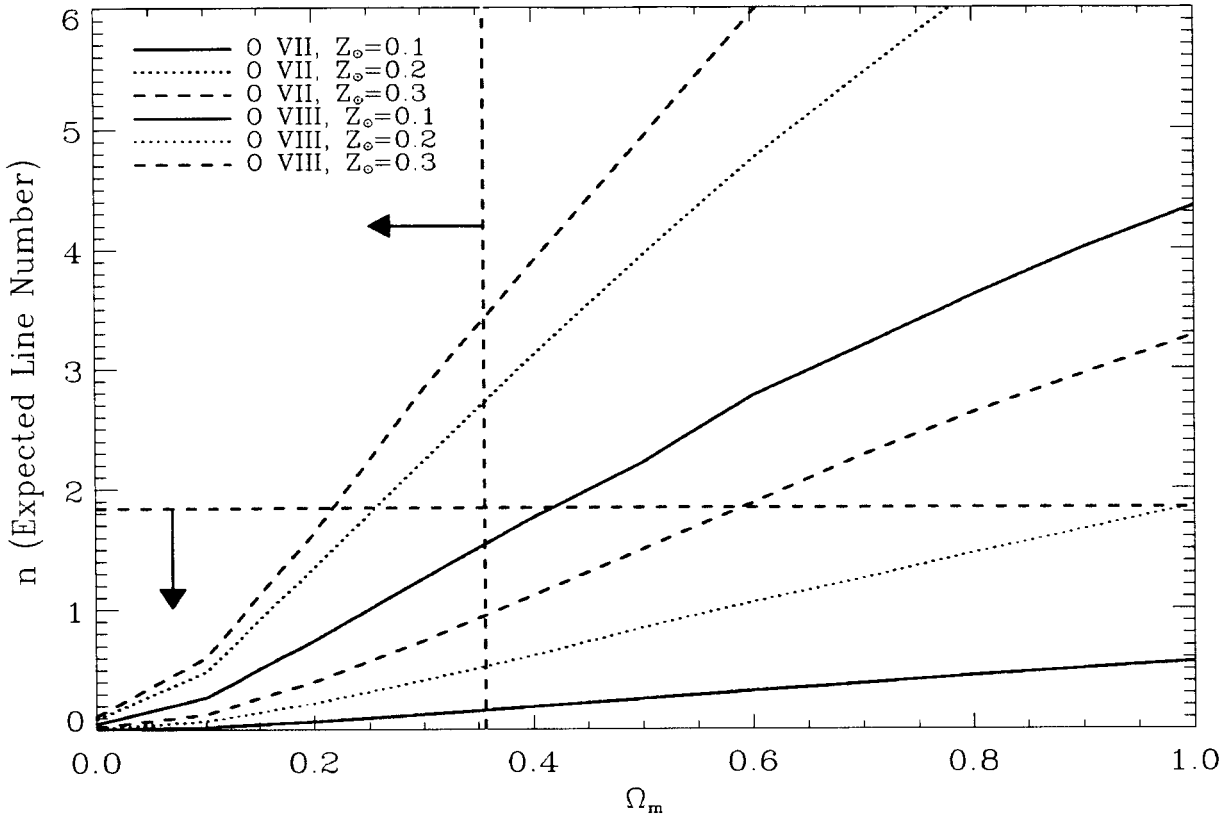

Fig. 11.— the expected total O VII (dark lines) and O VIII (red lines) line numbers with different Ω_m and metal abundance Z. The horizontal green line show the 1-σ upper limit from the no detection of absorption line in our sample. The vertical green line shows the value of Ω_m measured with *WMAP* (Spergel et al. 2003). The green arrows indicate allowed regions.

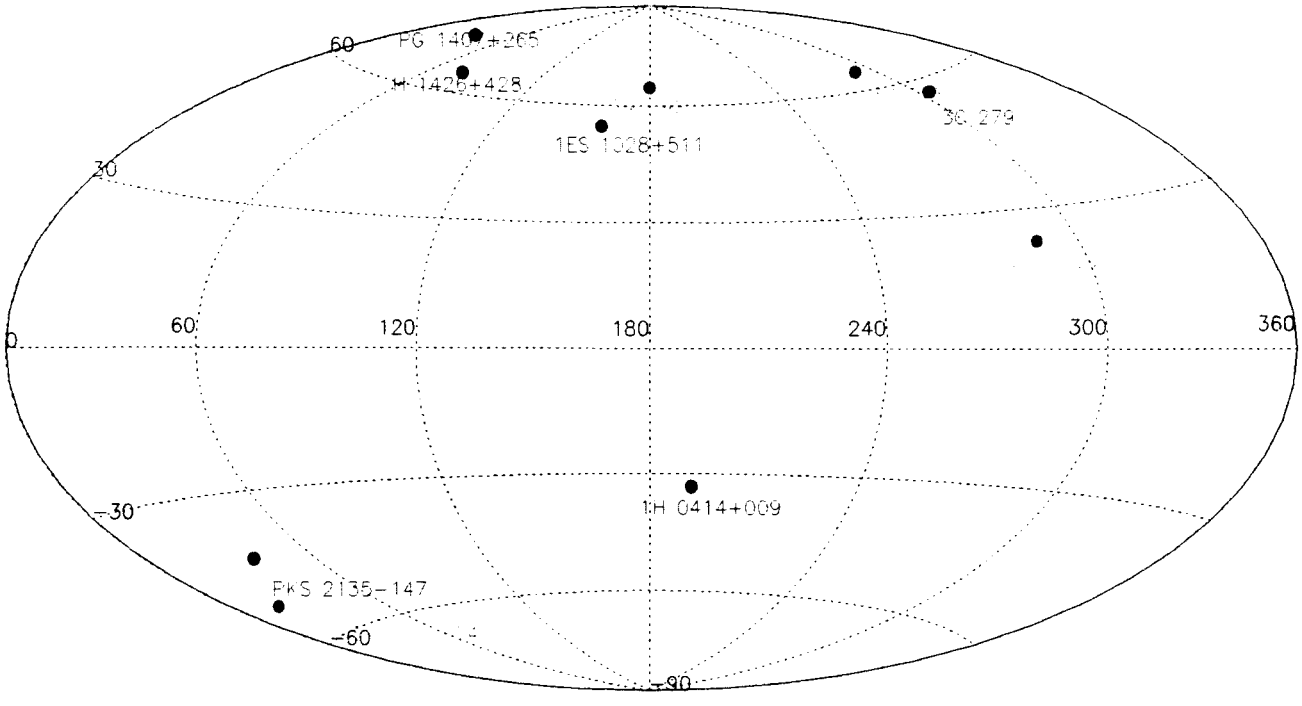

Fig. 12.— All-sky projection of quasars with known Galactic absorption lines (blue) and the six quasars in our sample (red).

REFERENCES

Blustin, A. J., Page, M. J., & Branduardi-Raymont, G. 2003, A&A, accepted (astro-ph/0312599)

Chen, X., Weinberg, D. H., Katz, N., & Davé, R. 2003, ApJ, 594, 42

Comastri, A., Fossati, G., Ghisellini, G., & Molendi, S. 1997, ApJ, 480, 534

Costamante, L. et al. 2001, A&A, 371, 512

Falomo, R., Pesce, J. E., & Treves, A. 1993, AJ, 105, 2031

Fang, T., Bryan, G. L., & Canizares, C. R. 2002, ApJ, 564, 604

Fang, T., Marshall, H. L., Lee, J. C., Davis, D. S., & Canizares, C. R. 2002, ApJ, 572, L127

Fang, T., Sembach, K. R., & Canizares, C. R. 2003, ApJ, 586, L49

Ganguly, R., Bond, N. A., Charlton, J. C., Eracleous, M., Brandt, W. N., & Churchill, C. W. 2001, ApJ, 549, 133

Gower, A. C. & Hutchings, J. B. 1984, AJ, 89, 1658

Hamann, F., Beaver, E. A., Cohen, R. D., Junkkarinen, V., Lyons, R. W., & Burbidge, E. M. 1997, ApJ, 488, 155

Hellsten, U., Gnedin, N. Y., & Miralda-Escudé, J. 1998, ApJ, 509, 56

Houck, J. C. & Denicola, L. A. 2000, ASP Conf. Ser. 216: Astronomical Data Analysis Software and Systems IX, 9, 591

Lanzetta, K. M., Wolfe, A. M., & Turnshek, D. A. 1995, ApJ, 440, 435

Madejski, G. et al. 1992, Frontiers Science Series, 583

Mathur, S., Weinberg, D., & Chen, X. 2002, ApJ, 582, 82

Marshall, H. L., Cheung, T., Canizares, C. R., & Fang, T. 2003, American Astronomical Society Meeting, 202

Miley, G. K. & Hartsuijker, A. P. 1978, A&AS, 34, 129

Nicastro, F. et al. 2002, ApJ, 573, 157

Polomski, E., Vennes, S., Thorstensen, J. R., Mathioudakis, M., & Falco, E. E. 1997, ApJ, 486, 179

Rachen, J. P., Mannheim, K., & Biermann, P. L. 1996, A&A, 310, 371

Rasmussen, A., Kahn, S. M., & Paerels, F. 2003, ASSL Vol. 281: The IGM/Galaxy Connection. The Distribution of Baryons at z=0, 109

Reeves, J. N. & Turner, M. J. L. 2000, MNRAS, 316, 234

Remillard, R. A., Tuohy, I. R., Brissenden, R. J. V., Buckley, D. A. H., Schwartz, D. A., Feigelson, E. D., & Tapia, S. 1989, ApJ, 345, 140

Sambruna, R. M. 1997, ApJ, 487, 536

Sambruna, R. M., George, I. M., Madejski, G., Urry, C. M., Turner, T. J., Weaver, K. A., Maraschi, L., & Treves, A. 1997, ApJ, 483, 774

Savage, B. D., Tripp, T. M., & Lu, L. 1998, AJ, 115, 436

Simcoe, R. A., Sargent, W. L. W., & Rauch, M. 2002, ApJ, 578, 737

Singh, K. P., Rao, A. R., & Vahia, M. N. 1991, A&A, 243, 67

Tripp, T. M. & Savage, B. D. 2000, ApJ, 542, 42

Tripp, T. M., Savage, B. D., & Jenkins, E. B. 2000, ApJ, 534, L1

Ueda, Y., Ishisaki, Y., Takahashi, T., Makishima, K., & Ohashi, T. 2001, ApJS, 133, 1

Whitney, A. R. et al. 1971, BAAS, 3, 465

Wilkes, B. J. & Elvis, M. 1987, ApJ, 323, 243

Wolter, A. et al. 1998, A&A, 335, 899

Wood, K. S. et al. 1984, ApJS, 56, 507

This manuscript was prepared with the AAS LaTeX macros v5.0.